

Reduced Drying Time of Anodes for Lithium-Ion Batteries through Simultaneous Multilayer Coating

Jana Kumberg,* Werner Bauer, Joyce Schmatz, Ralf Diehm, Max Tönsmann, Marcus Müller, Kevin Ly, Philip Scharfer, and Wilhelm Schabel

The extended process chain starting from slurry mixing up to the operative lithium-ion battery requires a deep understanding of each individual process step and knowledge of the interaction of the different process steps with each other. In particular, the intertwining of slurry mixing and drying determines the microstructure of the electrode, which in turn affects the performance of the cell. Herein, a scalable multilayer approach is used to tailor electrodes with improved mechanical and electrochemical properties, which disclose their advantages especially at high drying rates. Cryogenic broad ion beam scanning electron microscopy (Cryo-BIB-SEM) micrographs are used to reveal the influences of different process parameters, like slurry formulation, mixing device, and properties of the active material on the intrinsic network between active particles and binders in graphite-based anode slurries. By a chosen combination of these slurries in a multilayer electrode, a tenfold acceleration of the drying time with favorable mechanical and electrochemical properties for full cells derived from these anodes is demonstrated.

Diehm et al.^[2] Up to now, however, acceleration of drying through higher drying rates is usually accompanied by a deterioration of the electrode properties.^[2,3] This was proven to be caused by additives like binder or carbon black accumulating at the surface of the electrode and depleting at the current collector–particle interface.^[4,5] The additives are transported to the surface by capillary transport along with the solvent, with the amount of redistributed additives depending on the applied drying rate.^[6–9] In water-based anodes, a binder system comprising the thickener carboxymethyl cellulose (CMC) and the adhesion promoting latex binder styrene–butadiene rubber (SBR) is commonly used. The binding mechanism between CMC, SBR, and the active material has been investigated for various systems.^[10–16] CMC was found to form a network at contents of around 2 wt% CMC in the dry composite.^[17]

It was further found that the bonding mechanism between CMC and the active material depends on the surface properties of the active material. This is attributed to the interaction either between the CMC backbone and a more orderly surface of graphite, dominated mainly by Van der Waals forces, compared with a stronger binding force between the functional carboxylic groups of the CMC and a more disordered lateral surface with protruding edges and a higher likelihood to form –OH groups on the graphite surface. Formation of ester bonds was shown with these –OH groups, leading to a strong crosslinking between binder and active material and a suppressed binder migration.^[13] A difference between the distribution of the SBR binder and that of the CMC was found using time of flight–secondary-ion mass spectrometry (TOF–SIMS) mapping depending on the surface properties of the graphite.^[13] Different networking behaviors of CMC and graphite particles were observed by Lim et al. depending on the mass fraction of CMC. Furthermore, it was shown that SBR only is adsorbed on graphite particles at very low concentrations of CMC in the slurry by means of rheological investigations as well as by cryo–SEM.^[14] The choice of CMC in terms of substitution degree (DS) and molecular weight is another factor that has to be taken into account regarding the adsorption behavior of CMC onto graphite.^[18] While the binder system and especially the choice and the mass fraction of CMC influence the networking behavior and thus the properties of the slurry, another important impact factor on that matter is the conductive agent carbon black. It was shown that the mass fraction as well as the bound fraction in contrast to the free fraction of


1. Introduction

The drying speed in the production of electrodes for lithium-ion batteries is still a limiting factor in cell production.^[1] The coating step, which is usually conducted by slot-die coating, could be accelerated to much higher coating speeds, as shown by

J. Kumberg, R. Diehm, M. Tönsmann, K. Ly, P. Scharfer, W. Schabel
Karlsruhe Institute of Technology (KIT)
Light Technology Institute (LTI)
Thin Film Technology (TFT)
Straße am Forum 7, Karlsruhe D-76131, Germany
E-mail: jana.kumberg@kit.edu

W. Bauer, M. Müller
Karlsruhe Institute of Technology (KIT)
Institute for Applied Materials – Energy Storage Systems (ESS)
Hermann-von-Helmholtz-Platz 1, Eggenstein-Leopoldshafen 76144,
Germany

J. Schmatz
MaP—Microstructures and Pores GmbH (MaP)
Lochnerstraße 4-20, Aachen D-52064, Germany

 The ORCID identification number(s) for the author(s) of this article can be found under <https://doi.org/10.1002/ente.202100367>.

© 2021 The Authors. Energy Technology published by Wiley-VCH GmbH. This is an open access article under the terms of the Creative Commons Attribution License, which permits use, distribution and reproduction in any medium, provided the original work is properly cited.

DOI: 10.1002/ente.202100367

carbon black defines the gel strength of cathode slurries and thereby the electrode conductivity. It was further found that the electrode rate capability does not necessarily correlate with the electric conductivity.^[19] It was also reported that processing conditions like shear force during electrode coating and temperature during drying influence cell performance.^[20]

In summary, the local state of the material on the molecular level influences bonding mechanisms and thus electrode properties. This influence does not only evolve from the actual material specifications but also from their impact on the subsequent processing steps. For cathodes, an influence of the mixing step on cell performance was shown caused by a higher deagglomeration of the carbon black, combined with a more intensive kneading of binders onto the active material using a high shear-mixing process.^[21,22] As a result, the network of additives and active material within the slurry leads to a different microstructure of the dry electrode, which is later formed during the drying step. As a logical consequence, the slurry itself could be tailored to meet specific demands within the electrode. It is known that binder is needed to guarantee a certain adhesion of the electrode onto the substrate foil for reliable industrial-scale electrode fabrication—a reduction of the binder amount in the electrode is in contrast advantageous for the cell performance. The usage of a primer layer in the interface to the current collector is a measure of improving adhesion despite a low binder content.^[2] However, the application of a primer layer necessitates an additional coating and drying step. Simultaneous coating of two wet slurries with differing properties on top of each other is a more efficient approach, as only one coating and drying step is required. Good adhesion can be achieved using a higher binder amount in the lower layer, and a performance-enhancing low binder content can be used in the top layer. It was shown that improved cell performance occurs if multilayer anodes are processed simultaneously, with the bottom layer, containing all of the SBR binder.^[23] It was also shown that the use of two-layered cathodes leads to improved cell performance.^[24]

In this work, the multilayer approach is applied for anode slurries with a suppressed tendency for binder migration in the bottom layer to obtain high adhesion forces, combined with a top layer with improved electrochemical performance. This approach allows for very high drying rates, whereas the electrode still possesses good mechanical and electrochemical properties compared with a single-layered reference graphite anode, dried under the same conditions.

2. Properties and Interaction of Slurry Components

Four slurries were prepared, as explained in more detail in the Experimental Section. These slurries are compared with a reference slurry with regard to slurry formulation, mixing device, and properties of the active material.

2.1. Slurry Characteristics

The reference process is a mixing step in a dissolver mixer using a nonspherical graphite powder with d_{50} of 18.4 μm and with a total amount of active material of 40 wt% in the slurry. This reference slurry is furthermore denoted with (R). Three additional slurries are derived from the reference recipe, as shown in **Table 1**. As representative for a different particle shape, a spherical graphite (hereafter referred to as (S)) with a d_{50} of 10.3 μm is processed in an identical mixing procedure. To investigate the influence of the shear stress introduced during the mixing process, a pilot-line kneading device (hereafter called (K)) is used instead of the small laboratory dissolver. As reduced binder amounts have been reported to positively affect the cell performance, the fourth slurry is prepared with reduced amounts of additives, that is, the amounts of CMC, SBR, and carbon black are decreased (slurry (A)).^[2]

2.2. Slurry Structure

The choice of the active material as well as the mixing procedure deeply influences the microstructure of the slurry and the dry electrodes in consequence. Knowledge of this structure supports the understanding of the interactions between the active material and the additives. Therefore, the microstructure of the different slurries prior to drying was illuminated by cryo–broad ion beam (BIB)–SEM, as shown in **Figure 1**, similar to the approach described by Jaiser et al.^[9] The network built by the active material and the binder is clearly visible in these micrographs. For better understanding, some exemplary structures formed by the CMC network in the respective slurries are highlighted in each overview image (red rectangles).

2.2.1. Reference: Slurry (R)

Dissolver for Mixing, Nonspherical Graphite: In slurry (R) (**Figure 1a**, centre), the nonspherical graphite particles can be observed, embedded in a CMC network, which seems to be composed of small rectangular cells. The network has similarity to pictures reported by Lim et al. (2015).^[14] Close-ups of slurry (R) show the connections between CMC and graphite (**Figure 1a**, left), and a more detailed view of the CMC network (**Figure 1a**, right) reveals its coverage with SBR beads. Due to the cryo conditions, the SBR latex still exists in the form of individual spheres and has not coalesced into a film yet. In all samples, the SBR seems to adsorb preferably onto the CMC, whereas only a smaller fraction of SBR beads can be found on edges and protrusions of the graphite particles. Carbon black is mainly affiliated to the CMC/SBR network. This correlates with work in literature, where it was shown that CMC competitively occupies

Table 1. Denotation and differentiation of the four different slurries used in this work.

	Reference (R)	Spherical (S)	Kneader (K)	Additive reduced (A)
Graphite	Nonspherical	Spherical	Nonspherical	Nonspherical
Mixing device	Dissolver	Dissolver	Kneader	Dissolver
Active material content wt%	93	93	93	95.43

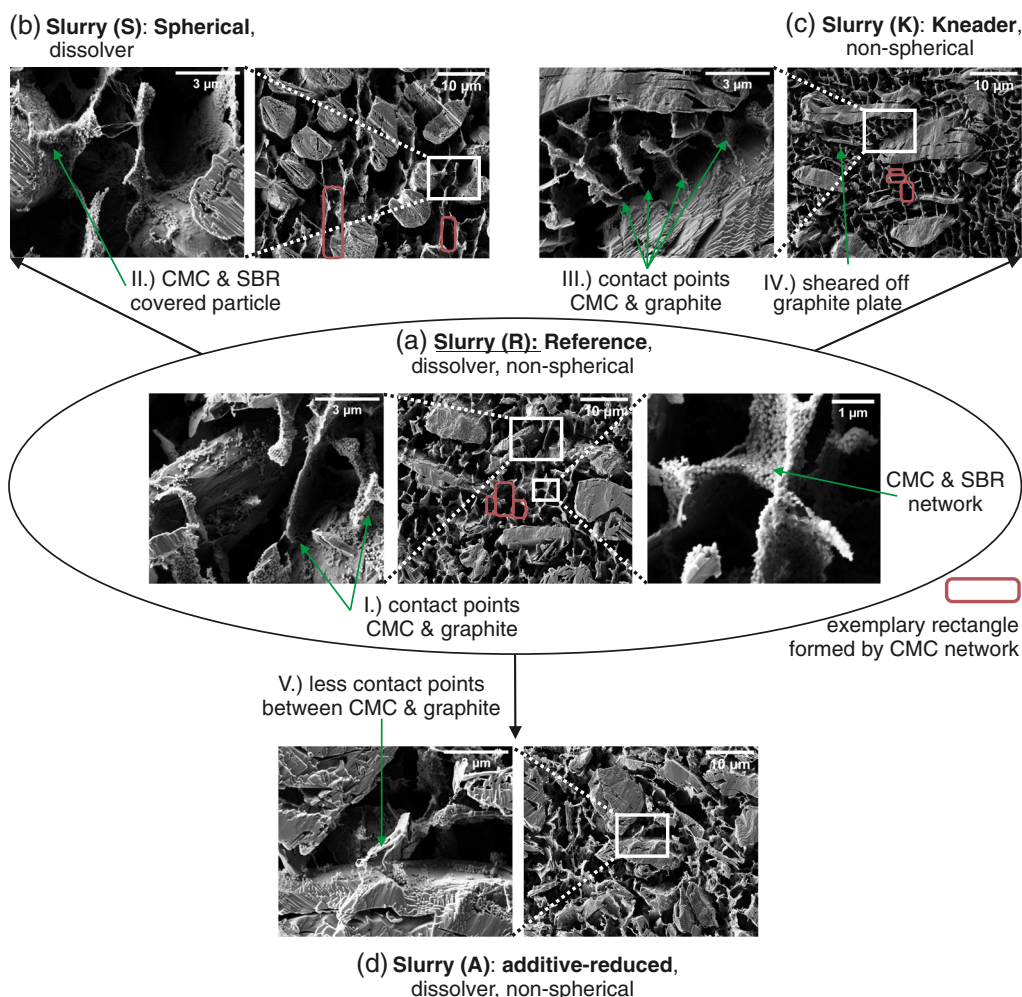


Figure 1. Cryo-BIB-SEM micrographs with overview images and close-ups of the four different slurries denoted in Table 1. Where a CMC network could be identified, exemplary structures are illuminated by red rectangles. Relevant descriptions from the text are marked by green arrows.

the graphite particles.^[12] A more detailed SEM image of the reference slurry is shown in **Figure 2**, with further micrographs of all slurries also included in Figure S5–S9, Supporting Information.

2.2.2. Change of the Active Material: Spherical Graphite: Slurry (S)

Change of the Particle Size (Distribution), Particle Shape, and Surface Chemistry: The CMC structure in the spherical graphite containing slurry (S) (Figure 1b, right and **Figure 3**) differs from the other slurries. The CMC chains seem to be more elongated with not only point-like contacts but the appearance of planar adsorption along the graphite surface (Figure 1b, left, II). A possible explanation for the different adsorption behaviors of the CMC on the spherical and the nonspherical graphite can be derived from Raman measurements (**Figure 4**). In the case of the spherical graphite, a pronounced D-peak in the Raman spectrum was measured, indicating a disordered crystal structure that is prone to provide OH groups at its surface, as described by

Chang et al.^[13] In addition to the increasing number of bonding sites with the carboxyl groups of the CMC, these OH groups are also capable of establishing strong ester bonds, which might further promote fixation of the polymer on the graphite surface. A larger amount of the binder could therefore adhere on the surface of the graphite, whereas the mobile fraction in the interstices between the graphite particles would be smaller. In the case of the nonspherical graphite, an unremarkable D-peak was measured, suggesting adsorption being mainly governed by weak Van der Waals forces.

2.2.3. Change of the Mixing Device: Kneader: Slurry (K)

Change of the Particle Size (Distribution), Particle Shape, and Surface Chemistry: The SBR–CMC network in the slurry derived from the kneading process (K) (Figure 1c, right and **Figure 5**) is more branched and reveals more contact points between CMC and graphite particles (Figure 1c, III) than the dissolver reference slurry (R). A relevant aspect is the partial grinding of the active material, as graphite layers being sheared off from the huge

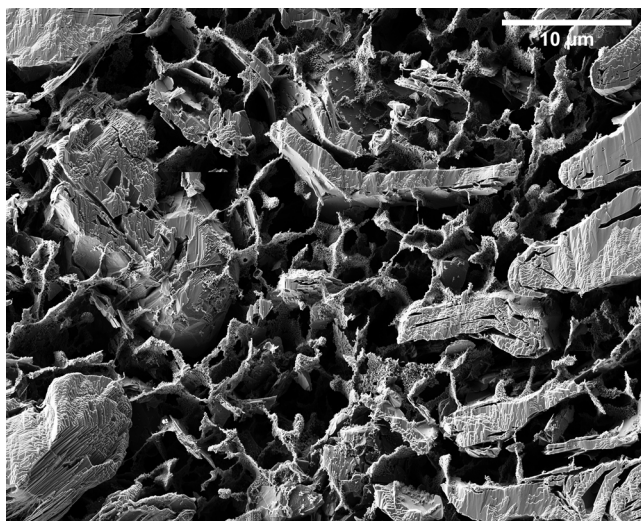


Figure 2. Cryo-BIB-SEM micrograph of the reference slurry (R).

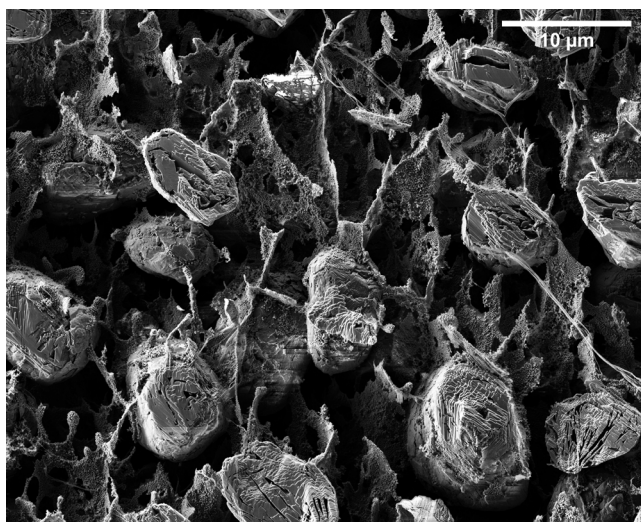


Figure 3. Cryo-BIB-SEM micrograph of slurry (S) with a different, spherical-shaped active material.

particles can be found as small plates in the slurry (Figure 1c, IV). In the large kneading machine, higher shear forces are produced despite the higher rotational speed of the dissolver. This is caused by the three twisted blades of the kneader, rotating around the centrum; meanwhile, each blade rotates around their respective axes, thus generating a very small gap and high shear forces between the container and the mixing tools. In addition, high shear forces are induced due to the mixing procedure starting at very high viscosities. This is reflected in the particle size distribution, which decreased to $15.4\ \mu\text{m}$ for the d_{50} of the kneader slurry compared with $17.24\ \mu\text{m}$ for the reference slurry, whereas the pristine nonspherical graphite had a nominal d_{50} of $18.4\ \mu\text{m}$ (see Figure S1, Supporting Information). Higher shear forces were reported to additionally intensify the deagglomeration of carbon black, producing a larger number of nanosized fragments.^[22] This impacts the rheology due to more distinct binder bridging,^[25] leading to a gel-like behavior of slurry (K),

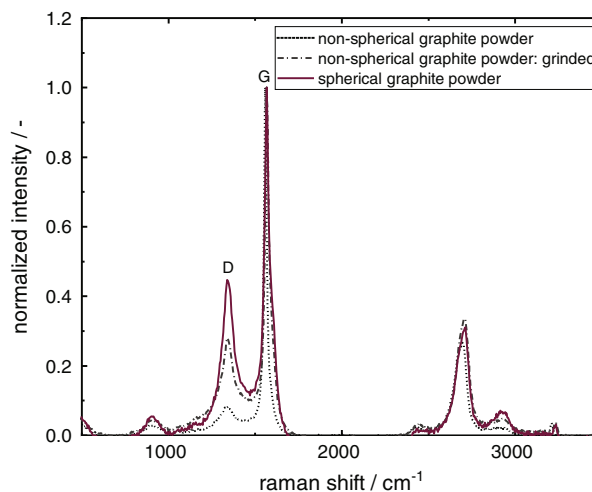


Figure 4. Raman spectra of the nonspherical and spherical graphite powders used for electrode fabrication in this work, as well as Raman spectrum of ground nonspherical graphite powder. Spectra are normalized to the maximum intensity of each spectrum.

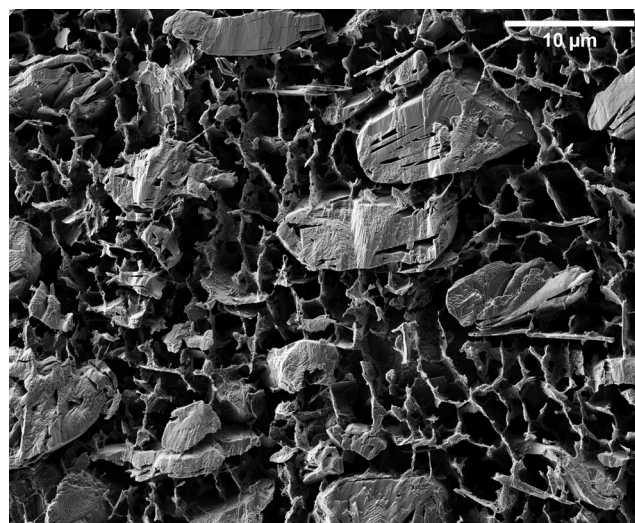


Figure 5. Cryo-BIB-SEM micrograph of slurry (K) originating from a different mixing process in the kneader.

while slurry (R) still shows a liquid-like behavior (see dynamic viscosity as a function of the shear rate and phase-shift angles at different angular frequencies in Supporting Information, Figure S2 and S3, Supporting Information). Extended bridging due to the higher number of small particles could also explain the smaller cell size of the CMC network in slurry (K). Another factor, which might influence the adsorption of CMC onto graphite, is shown in Figure 4: After manual grinding of the nonspherical graphite, the Raman spectrum shows a more pronounced D-peak than the pristine nonspherical graphite powder. As described in Section 2.2.4, this can promote fastening of the polymer on the graphite surface, leading to the observed higher number of contact points between the graphite and the CMC. Similar results were found for cathode slurries mixed in the kneader, with a

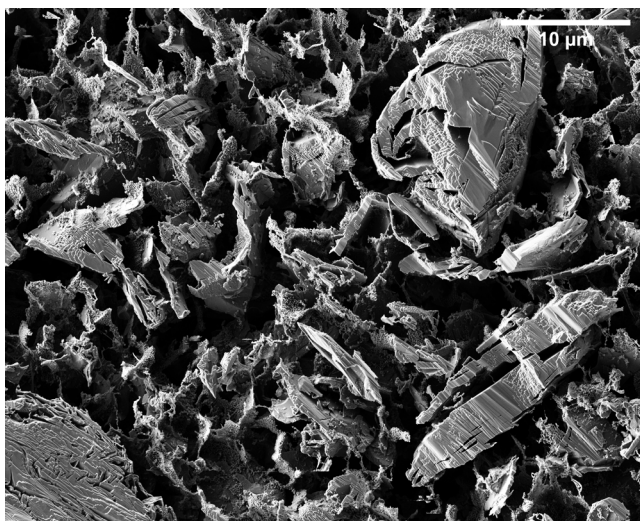


Figure 6. Cryo-BIB-SEM micrograph of slurry (A) originating from a formulation with a reduced amount of the additives CMC, SBR, and carbon black.

higher adsorption of PVDF onto NMC particles, as described by Bockholt et al.^[22]

2.2.4. Change of the Recipe: CMC, SBR, and Carbon Black Additive Reduction: Slurry (A)

For an additive-reduced slurry (A) (Figure 1d and 6), fewer contact points to the graphite particles can be observed compared with the reference slurry (R). In addition, the CMC/SBR network in the interstices between the graphite particles seems to be

developed only marginally (Figure 1d). Most of the binder seems to be fixed on the surface of the graphite instead of participating in the binder network between the graphite particles.

3. Single-Layer Electrodes

The slurries were coated and dried in an impingement batch dryer, as described in the Experimental Section. To discern the impact of the drying rate on the electrodes, the drying rate was varied between 0.5 and $2.2 \text{ g m}^{-2} \text{ s}^{-1}$. The drying rates were experimentally confirmed and thus represent actual values to derive the real drying time. More details are given in the Supporting information (Figure S4, Supporting Information).

3.1. Adhesion Force and Electrical Conductivity

The coated slurries were dried at drying rates of 0.5 and $2.2 \text{ g m}^{-2} \text{ s}^{-1}$ and the resulting adhesion force as well as their electrical conductivity was measured (Figure 7). The corresponding area capacities lie between 2.0 and 2.4 mAh cm^{-2} with an average value of 2.2 mAh cm^{-2} . The exact values are shown in Table S1, Supporting information.

3.1.1. Electrode (R): Reference

Electrode (R) shows a decrease in the adhesion force as well as electrical conductivity when a higher drying rate is applied. These findings correlate with the literature, where a decrease in the adhesion force at a higher drying rate was reasoned with binder migration.^[3,6–8,26] The decrease in electrical conductivity fits well into this reasoning, under the assumption that a binder carbon

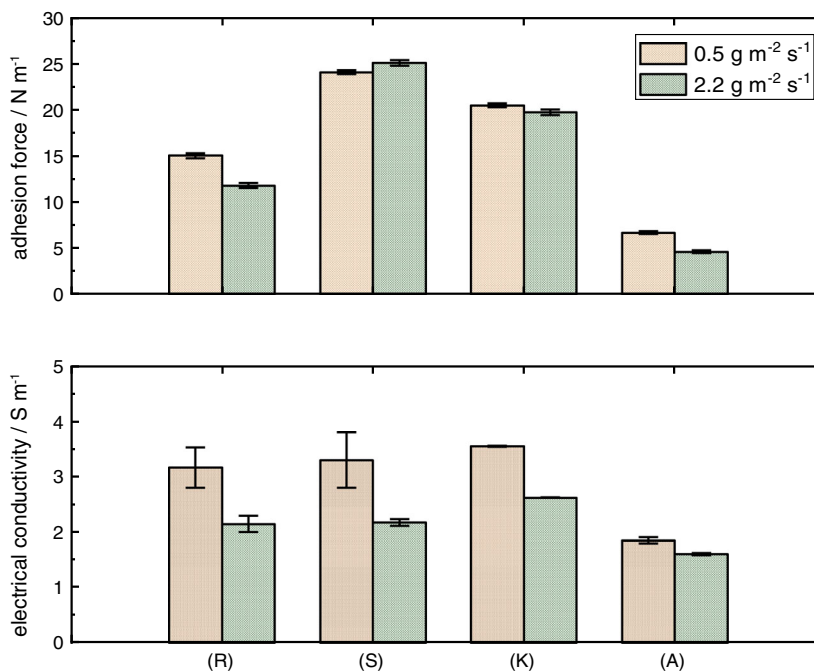


Figure 7. Adhesion force (top) and electrical conductivity (bottom) of single-layer electrodes. All electrodes were dried at a drying rate of 0.5 and $2.2 \text{ g m}^{-2} \text{ s}^{-1}$, respectively.

black network is present in the slurry, which migrates collectively during drying.^[25] This would result in a more inhomogeneous microstructure, leading to fewer electrical pathways and reduced electrical conductivity, especially when electrodes are dried at higher drying rates.

3.1.2. Electrode (S): Change of the Active Material to a Spherical-Shaped Graphite

Electrode (S) has a significantly higher adhesion force and a matching electrical conductivity compared with the reference (R). While it shows the same drop in electrical conductivity, the adhesion is even slightly improved at the higher drying rate, which might lead to the conclusion that either the mechanism of binder migration is not present or that it is superimposed by some other effect. Based on Section 2.2.2, this additional effect, which might lead to an increase in the adhesion strength, could be indicative of more binding sites on the surface of the spherical graphite and stronger ester bonds, which are formed between the CMC and the active material during drying. The formation of strong ester bonds would be favored at an increase in the drying rate as in this work this is achieved by an increase in the film temperature from 30 to 50 or 65 °C, respectively (see Experimental Section for more details). With stronger fixation of the CMC on the graphite particles and the assumption, that SBR adheres on the CMC, the mobile fraction of the binder would be smaller, thereby reducing binder migration. Based on the cryo-BIB-SEM pictures, carbon black particles are also associated with the CMC and SBR clusters. However, their interaction seems to be based on weaker Van der Waals forces.^[27–29] This might allow carbon black transport by the capillary drag forces during pore emptying, independent of the binder, and could therefore explain the reduced electrical conductivity at the higher drying rate. It cannot be excluded that this is also valid for the SBR latex particles to some extent. They seem to adhere primarily to the CMC molecules based on the cryo-BIB-SEM micrographs but could retain a higher mobility in the slurry as long as film formation does not fixate them at the place. It can therefore be hypothesized that some mobile SBR binder is transported to the electrode surface during drying as well.

3.1.3. Electrode (K): Change of the Mixing Device to a Kneader

The kneader-produced electrode (K) also has a higher adhesion force compared with the reference (R) as well as a comparable electrical conductivity. A reason for the higher level of adhesion and conductivity compared with the reference could be abraded

graphite particles and a better dispersion of carbon black. The hypothesis here is that this results in a gel-type slurry with extended bridging and more contact points between CMC and the graphite particles, as explained in Section 2.2.3. This could also be overlaid by the impact of the stronger binding of the functional groups of the CMC to a more disordered surface of the stressed graphite. This reasoning would be consistent with the higher adhesion force due to a reduced mobility of the binder and lesser binder migration.

3.1.4. Electrode (A): Change to an Additive-Reduced Recipe

The basic level of adhesion and electrical conductivity of electrode (A) are lower compared with reference (R), as would be expected due to the reduced number of additives (see Table 2 in Experimental Section). Like for reference (R), adhesion and electrical conductivity are reduced with an increase in the drying rate.

3.2. Electrochemical Properties

Figure 8 shows the influence of the drying rate on the electrochemical performance for full coin cells with graphite anodes dried at 0.5 and 2.2 g m⁻² s⁻¹.

Differences between the four anodes are the most pronounced at a C rate of 3 C. This would be expected based on findings in literature and under the hypothesis that binder preferentially accumulates on electrochemically active sites. This would result in an increased hindrance of the phase transfer, which is particularly noticeable at high current strengths.^[2,3,10] Cell (A), derived from the additive-reduced slurry, has the highest discharge capacity, which is in good agreement with other findings in literature.^[2] Both cells (K) and (S) show a lower specific discharge capacity than the reference (R) over all C rates. The spherical graphite particles in the cell (S) have a higher Brunauer, Emmett, and Teller (BET) surface area of 3.7 m² g⁻¹ compared with the reference (R) with a BET surface area of 2.7 m² g⁻¹. A similar effect could be the reason for the performance of cell (K): due to the grinding effect, the surface area increases. As the active surface area is covered by an SEI layer, the nonreversible lithium loss increases, which influences cell performance, as all cells are built with identical balancing. An increase in the drying rate to 2.2 g m⁻² s⁻¹ has a moderate beneficial impact on the discharge capacity of all cells, with cells (K) and (S) showing the strongest effect. Nevertheless, they do not surpass the electrochemical properties of the reference cell (R). The electrochemical performance thereby does not correlate either with the trends of

Table 2. Composition of dry electrodes.

Material	Composition of dry single-layer electrode [wt%]				Composition of dry multilayer electrode [wt%]		
	(R)	(S)	(K)	(A)	(A) @ top	(R) @ top	Primer @ bottom
Graphite SMGA	93	93	93	95.43	94.62	93	95.43
Carbon black	1.4	1.4	1.4	1.00	1.13	1.4	1.00
CMC	1.87	1.87	1.87	1.45	1.59	1.87	1.45
SBR	3.73	3.73	3.73	2.12	2.66	3.73	2.12

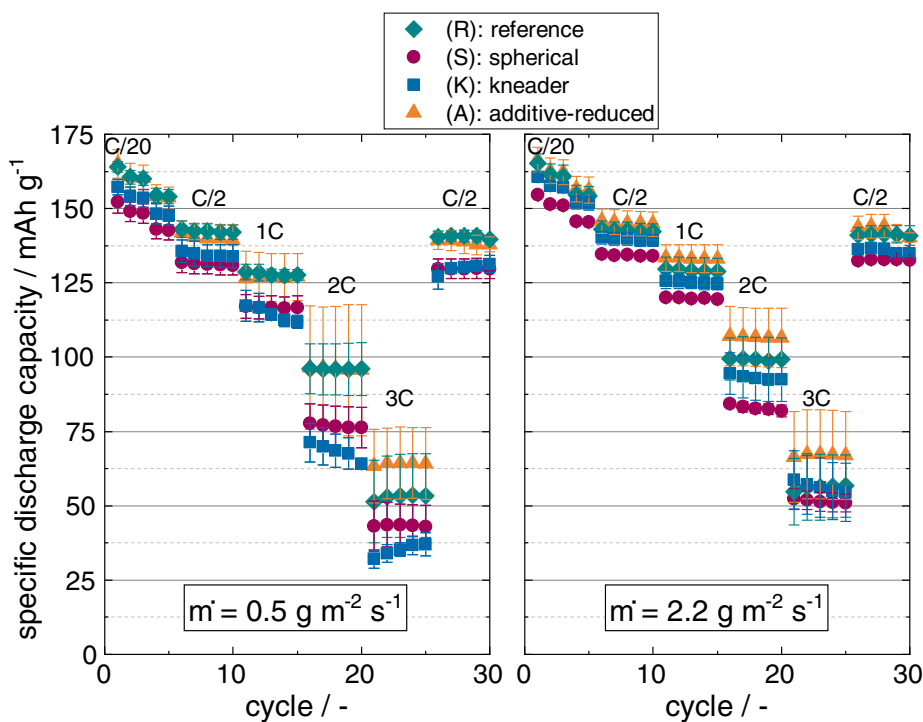


Figure 8. Rate tests depicting the specific discharge capacity of full coin cells with NMC622 cathodes built with single-layered anodes of the four slurries (R), (S), (K), and (A) processed at two different drying rates.

mechanical or electrical performance in terms of adhesion force and electrical conductivity measurements. This was also reported in literature by Morelly et al.^[19] Evidently, more complex inter-relationships are present which determine the cells rate capability. For a reference to a pouch cell test and cycle stability, the authors would like to refer to Diehm et al., with the electrode (A1 + A1) being identical to electrode (K) in this investigation.^[23]

4. Multilayer Electrodes

In the previous sections, it was shown that electrodes (K) and (S) have a preferential behavior regarding the adhesion properties but reveal the worst performance in C-rate tests. In contrast, electrode (A) shows the best electrochemical performance but the poorest adhesion. An absolute minimum of an adhesion strength of at least 6 N m^{-1} should be achieved according to Diehm et al.^[2] This value is always dependent on subsequent processing steps, which is why a value of at least 10 N m^{-1} was targeted here with the aim of defect-free industrial-scale handling. Therefore, a multilayer configuration was chosen to merge both good adhesion and electrochemical performance within one electrode. As accelerated drying is preferred in electrode production, the previously applied drying rates of 0.5 and $2.2 \text{ g m}^{-2} \text{ s}^{-1}$ are extended with another drying rate at $5 \text{ g m}^{-2} \text{ s}^{-1}$.

4.1. Layer Setup

The investigated multilayer configurations had area capacities between 2.3 and 2.6 mAh cm^{-2} with an average value of 2.5 mAh cm^{-2} . The exact values are shown in Table S2,

Supporting Information. All simultaneously coated multilayered electrodes consisted of a bottom layer being one-third of the total wet film thickness and a top layer being two-thirds of the total wet film thickness. The reduced tendency for binder migration behavior of slurry (K) and (S) makes them attractive as the bottom layer. They were combined with the additive-reduced top layer (A) that provided the best single-layer electrochemical performance. A primer layer in combination with slurry (A) as top layer was investigated for comparison with literature.^[2] In contrast to the other electrodes, the primer layer containing the electrode was processed in two steps as the primer layer was coated and dried first and the upper layer (A) was deposited on top of the dry primer layer.

Figure 9 shows an SEM micrograph of a dry electrode consisting of a bottom layer with the spherical graphite and a top layer with the nonspherical graphite. Separated layers are recognizable

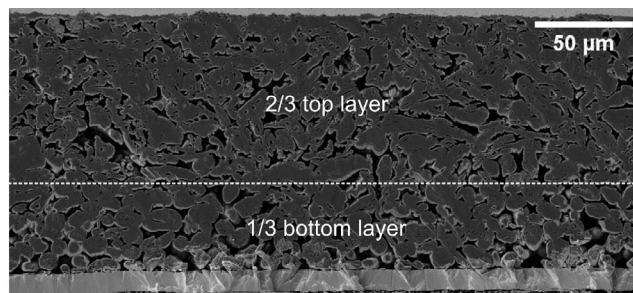


Figure 9. SEM picture of a multilayer electrode derived from the simultaneous coating of a bottom layer with a spherical graphite and a top layer of the reference slurry containing a nonspherical graphite.

despite the simultaneous coating of both layers on top of each other, indicating that vertical slurry intermixing during simultaneous two-layer coating was not an issue.

4.2. Adhesion Force and Electrical Conductivity

The resulting electrodes were tested for their adhesion force as well as their electrical conductivity. The results for the adhesion force are shown in **Figure 10** and the ones of the electrical conductivity in the Supporting Information (Figure S10, Supporting Information), with the corresponding theoretical capacities shown in Table S2, Supporting Information.

Both simultaneously coated multilayers (S || A) and (K || A) show very good adhesion properties at the low as well as at the high drying rate. The adhesion is close to the one of the respective bottom single layers and about a factor 2–3 higher than the one of the single top layers. As the multilayer coating consists of two films on top of each other, their respective thickness during coating is lower than the one of the single-layer films. A different electrode structure of the multilayer films compared with the single layers due to the increased shear rate of the thinner coatings, as was reported by Saraka et al., can therefore not be entirely excluded.^[20] This influence should be minimal though, based on measurements of the dynamic viscosity in the relevant range for coating (see Figure S2, Supporting Information).

The sequentially coated multilayer using a primer coating (primer || A) shows only a slight increase in adhesion force, which is almost neglectable, in contrast to the results reported by Diehm et al.^[2]

4.3. Electrochemical Properties

Cell tests of multilayer electrodes for the two drying rates of 0.5 and 2.2 g m⁻² s⁻¹ are compared in **Figure 11**. At a C rate of 3C, the multilayer with slurry (S) in combination with slurry (A) shows a similar discharge capacity as the one with the primer layer. Both electrodes reveal better properties than the reference sample (R) and the multilayer based on slurry (K) combined with slurry (A) at the low and the higher drying rate. The results show that high drying rates are accessible when using slurry (S) as bottom layer. In comparison with the single-layer electrodes, only the additive-reduced single layer (A) achieved a comparable rate capability but showed poor adhesion, limiting the suitability for industrial processing. The other single-layer electrodes provided higher adhesion force but performed worse in C-rate tests. The multilayer approach, however, retains good adhesion as well as good electrochemical properties exceeding the single-layer reference, even for an increased drying rate with drying time of around 30 s at an area capacity of about 2.0 mAh cm⁻².

5. High-Speed Drying

Due to the promising results of multilayer electrodes, the drying rate was further increased to 5 g m⁻² s⁻¹ to reach a drying time of only 14 s at an area capacity of 1.9 mAh cm⁻² (compare Figure S4, Supporting Information). This very high drying rate was applied for single layers of the slurries (R) and (S) as well as a multilayer electrode (R || S) with slurry (S) as bottom layer and slurry (R) as top layer.

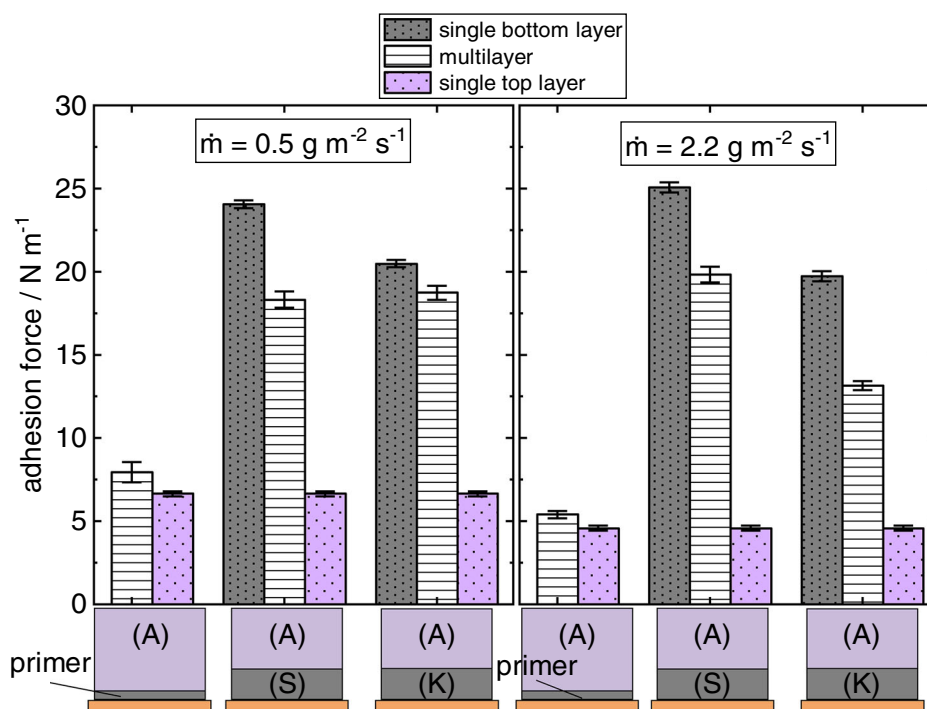


Figure 10. Adhesion force of the multilayer electrodes dried at two different drying rates of 0.5 and 2.2 g m⁻² s⁻¹. The corresponding properties of single bottom and top layers are given for comparison.

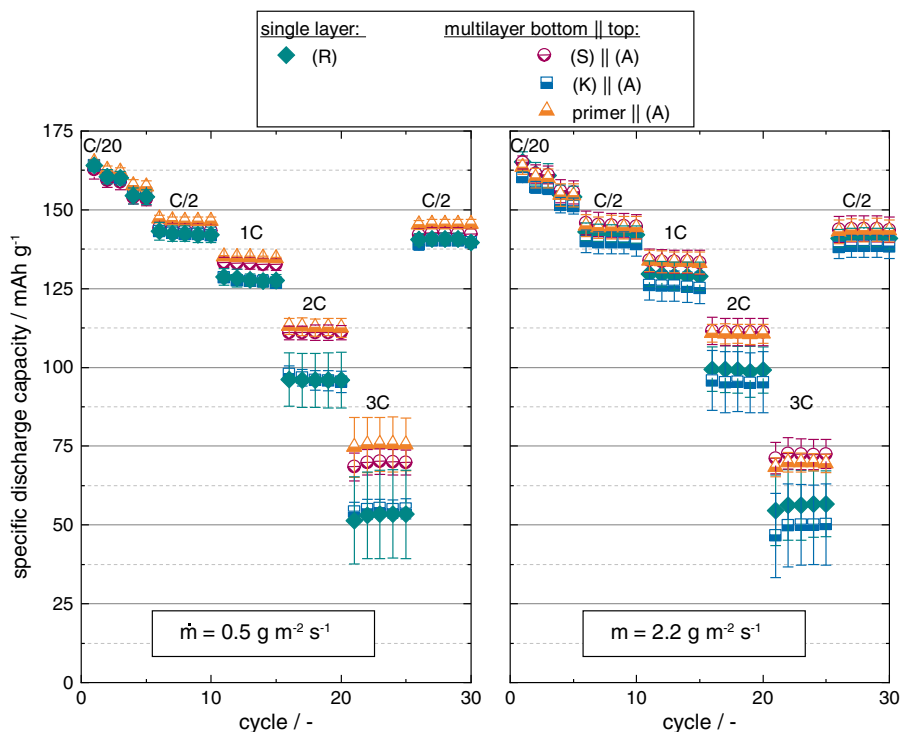


Figure 11. Cycle tests showing the specific discharge capacity of NMC622-based full cells made from multilayer anodes compared with a single-layer reference.

5.1. Adhesion Force and Electrical Conductivity

Adhesion results for high-speed drying are shown in **Figure 12**. The increase in the drying rate by a factor of 10 leads to a massive adhesion loss of the single-layer reference electrode (R) as expected. In contrast to this, slurry (S) coated as a single layer exhibits an increase in the adhesion force at the high-speed drying rate. This can again be reasoned with the hypothesis that an effective bonding mechanism occurs, as explained in Section 2.2.2. As the drying temperature of the low drying rate of $0.5 \text{ g m}^{-2} \text{ s}^{-1}$ was around 30°C and the one of the high-speed drying rate of $5 \text{ g m}^{-2} \text{ s}^{-1}$ was around 65°C , faster kinetics for the chemical reaction forming stronger ester bonds would be expected at the higher temperature. The multilayer electrode with slurry (S) as bottom layer gains an identical adhesion at the low drying rate as the corresponding single-layer electrode. However, the adhesion is slightly reduced for high-speed drying but still remains on a level far beyond the adhesion values of the reference slurry-based electrode (R). A possible explanation could be a change in the capillary transport due to different particle size distributions in the top and bottom layer caused by the two active materials. If the reaction rate for the formation of ester bonds was to compete with the drying rate and therefore with the speed at which water and binder are transported away from the formation site, a change in the pore radii distribution might change the capillary transport in the microstructure and thereby the available time for esterification.

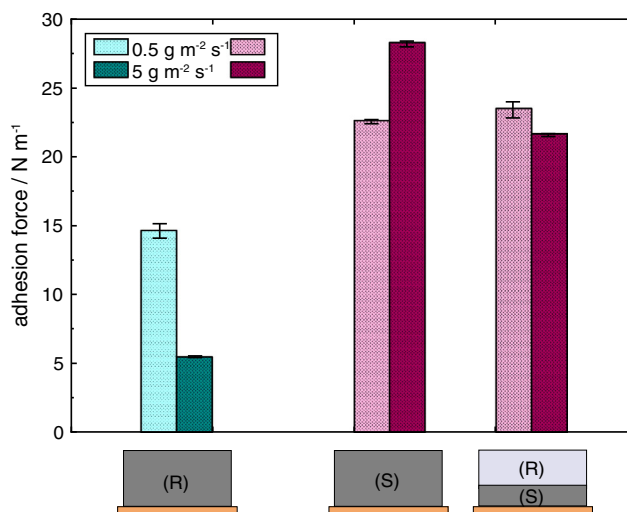


Figure 12. Adhesion force of slurry (R) and slurry (S) compared with a multilayer electrode derived from those two slurries. All electrodes were dried at a low drying rate of $0.5 \text{ g m}^{-2} \text{ s}^{-1}$ and a high-speed drying rate of $5 \text{ g m}^{-2} \text{ s}^{-1}$.

5.2. Electrochemical Properties

Full coin cell test results for high-speed drying are shown in **Figure 13**. Both single-layer electrodes (R) and (S) dried at $5 \text{ g m}^{-2} \text{ s}^{-1}$ exhibit reduced discharge capacities compared with the reference sample (R) dried at a much slower rate of 0.5 g m^{-2}

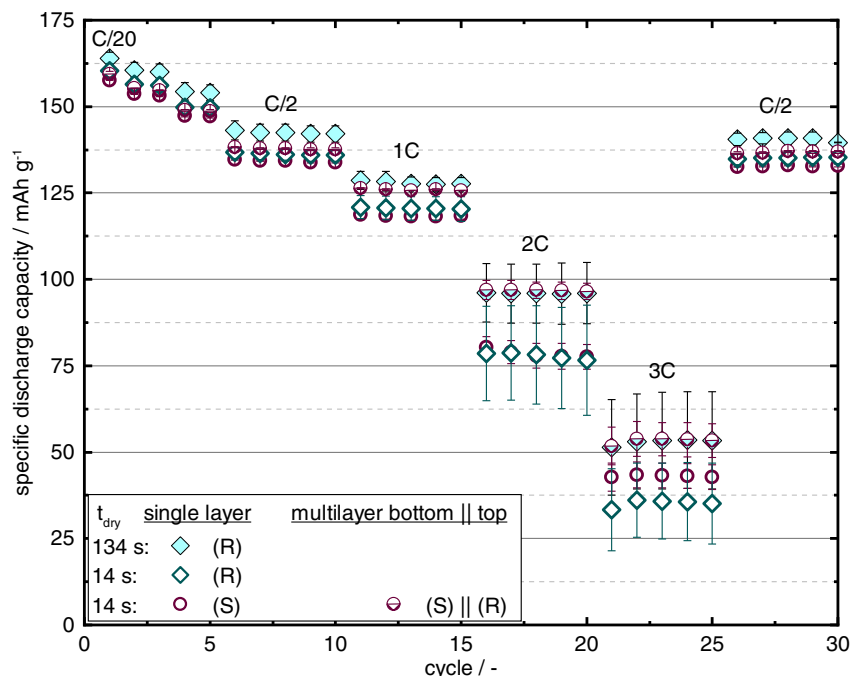


Figure 13. Specific discharge capacities of NMC622 full coin cells with a multilayer anode prepared at high-speed drying. Cells are compared with ones derived from single-layer electrodes with the corresponding compositions (S) and (R). Drying rates were varied between $0.5 \text{ g m}^{-2} \text{ s}^{-1}$ (134 s drying time) and $5 \text{ g m}^{-2} \text{ s}^{-1}$ (14 s drying time) and experimentally validated (see Figure S4, Supporting Information).

s^{-1} . The decline is particularly noticeable at high C rates at 1 C and beyond. The multilayer electrode dried at high speed shows a slight decrease at low C rates, which could be caused by the lower base capacity of the spherical graphite (see Section 3.2). However, at the higher C rates, it achieves discharge capacities, which are identical to that of the reference electrode (R) dried about 10 times more slowly.

6. Conclusion

The problem of increased binder migration during accelerated electrode drying is well-known from practical experience and from literature. In this work, the interrelationship between anode slurry properties, drying behavior, microstructure, and electrochemical performance was investigated to identify factors on the slurry level, which influence or even improve adhesion at higher drying rates. The most important findings in this work can be summarized as follows.

1) Different surface chemistries of the active material, different recipes, and different mixing techniques result in different slurry microstructures. This was shown using cryo-BIB-SEM technique. The interconnecting network of active material, carbon black, and the binder system CMC/SBR arising from four different slurries was visualized. Differences in the slurry microstructure were achieved by reducing the additive content, changing the mixing device from dissolver to kneader, as well as by changing the active material from a nonspherical to a spherical graphite.

2) Different slurry microstructures lead to electrode films with different adhesion strength and electrical conductivity. While an

additive reduction was found to generally lower the adhesion as well as the electrical conductivity of the electrode films, high adhesion strengths were observed for the electrodes derived from mixing with a kneader and when using the spherical-shaped graphite. It is hypothesized that the reason is a different adsorption between CMC and the active material, leading to the formation of strong ester bonds when a disordered graphite surface is provided. Different adsorptions of CMC on the active material were found in the cryo-BIB-SEM micrographs as well as a preferential adsorption of SBR on CMC.

3) Different slurry microstructures lead to electrode films which are differently affected by a variation of the drying process in terms of adhesion strength and electrical conductivity. In accordance with literature, a loss of adhesion strength and electrical conductivity was observed when the reference slurry and the additive-reduced one were dried at a higher drying rate.^[3,15] In contrast to that, high adhesion levels were found for the slurry mixed in the kneader and the one based on the spherical graphite dried at a high drying rate. The assumption again is that formation of ester bonds leads to the high adhesion force.

4) No clear correlation between adhesion strength, electrical conductivity, and electrochemical performance exists. An additive reduction is positive for the cell performance if a sufficient adhesion for industrial handling is reached. In cell tests, the additive-reduced slurry showed the best electrochemical performance despite low adhesion strength and electrical conductivity. The single-layer anodes with the highest adhesion strength and electrical conductivity, derived from the kneader and the spherical graphite, had the lowest specific discharge capacity in the cell test. As the additive-reduced anode outperformed the other ones

especially at the highest C-rate of 3C, it is assumed that the reason is higher mobility of lithium ions due to the lower additive content compared with the other electrodes.

5) Simultaneous coating and drying of two layers, one for adhesion and one for specific capacity, lead to improved films. To combine good mechanical properties, which are prerequisites for large-scale handling of the electrodes in a roll-to-roll-process, with beneficial electrochemical properties, a multilayer anode configuration was applied. A bottom layer of the slurry with improved adhesion strength, which was the one with the spherically shaped graphite, was combined with the top layer of the additive-reduced slurry. The multilayer showed discharge capacities surpassing the single-layer reference by around 25% at 3C and enabled a drying time of around 30 s at a theoretical area capacity of around 2 mAh cm⁻². Based on these results, a multilayer with the spherical graphite as bottom layer and the reference slurry as top layer was dried at an experimentally validated, extreme drying rate of 5 g m⁻² s⁻¹, which resulted in a drying time of only 14 s for the given area capacity. This multilayer showed the same discharge capacity at 3C as the reference electrode dried within 134 s, which is a tenfold acceleration of the drying time.

An additive reduction of the top layer of the high-speed-dried multilayer electrode is promising regarding the results shown in this work. Methods to determine the binder distribution and correlate it with processing conditions in realistic battery slurries while using the binder systems CMC and SBR are still sought and would be a valuable contribution. One method which is being investigated by the authors to undermine the hypothesis about differences in binder migration is laser-induced breakdown spectroscopy (LIBS), which has so far been used to detect the lithium distribution in cycled cathodes.^[30,31] High-speed drying could be implemented in pilot lines by utilization of IR radiators or lasers and product line speed increased by applying simultaneous multilayer coatings.

7. Experimental Section

In this section, the experimental procedures for slurry mixing, coating, drying, calendaring, as well as coin cell manufacturing and testing are explained in detail.

Anode Mixing: All slurries were prepared according to the recipes shown in Table 2 with a dry mass fraction of 43 wt% in the slurry. As a thickening agent, the same carboxymethyl cellulose (Sunrose MAC500LC CMC) was used, which was received from Nippon Paper industries, Japan, with a DS of 0.67 and a molecular weight of 349 000 g mol⁻¹. The CMC was dissolved in a first step in distilled water. The active material was either a nonspherical graphite with a d_{50} of 18.4 μm or a spherical graphite powder with a d_{50} of 10.3 μm (both from Hitachi Chemical Co. Ltd., Japan). The BET surface area of the spherical graphite was 3.7 m² g⁻¹ compared with that of the nonspherical graphite with 2.7 m² g⁻¹, measured by mercury intrusion porosimetry. Carbon black was Super C65 from Imerys, Switzerland. Slurry mixing was either conducted using a dissolver (VMA Getzman Dispermat CN10, Germany) or a kneader (TX-15, Inoue MFG., Japan).

Dissolver: Using the dissolver, the active material and carbon black were dry mixed first for 15 min at 300 rpm in a 0.8 l beaker with a 160 mm disk. The CMC solution and additional distilled water were added in two steps until the final composition was attained. The main mixing step lasted for

45 min at 1500 rpm. Afterward, the dispersion of SBR (Zeon Europe GmbH, Japan) was mixed into the slurry for 10 min at 500 rpm.

Kneader: In the kneader with a maximum volume of 15 l, a dry-mixing step of carbon black and active material was applied for 10 min at 25 rpm. The CMC solution and distilled water were added in three steps, until the final composition was reached. The following main mixing step lasted for 80 min at 104 rpm. The SBR was added in the last step followed by mixing for 10 min at a speed of 25 rpm.

The slurry temperature was controlled by water cooling the mixing vessel and degassing was executed during the main wet-mixing step in the dissolver and the kneader.

Anode Coating, Drying, and Calendaring: Each single-layered or multilayer anode was coated onto the copper foil (electrodeposited, 10 μm thickness, Civen Metal, China), resulting in electrodes of ≈1 m of length and a width of 0.06 m, as described in more detail by Diehm et al.^[23] For simultaneously coated multilayers, the wet film layer thickness ratio was one-third bottom layer to two-thirds top layer. Electrode drying was conducted in a batch-wise working impingement dryer with an array of 20 slot nozzles, as described by Baunach et al.^[32] The copper foil was fixed onto a temperature-controlled substrate support plate via a vacuum groove at the edges of the plate, ensuring a defined heat input. A stepper motor moved the heating plate with the coated film into the dryer chamber such that a coating speed of 6 m min⁻¹ occurred. A periodic movement beneath the slot nozzle array at a speed of 100 mm s⁻¹ ensured uniform drying. The drying rate was defined for all experiments by the temperature of the heating plate and the heat transfer coefficient of the slot nozzle dryer, while considering the dew point of the drying air, as explained in more detail in the study by Kumberg et al.^[33] The heat transfer coefficient was 35 W m⁻² K⁻¹ for all experiments. The temperature of the heating plate and the drying air were changed from around 30 °C, for a drying rate of 0.5 g m⁻² s⁻¹, to 50 °C for a drying rate of 2.2 g m⁻² s⁻¹, and to 65 °C for a drying rate of 5 g m⁻² s⁻¹. Calendaring was conducted using a hot-rolling press (GN MR 100 H from Gelon, China), resulting in porosities of ≈45%, which are shown in Table S3 and S4, Supporting Information.

Powder Characterization: Inverse micro-Raman spectroscopy (IMRS), comprising a confocal Raman system (Labram, Jobin Yvon) coupled with an inverse microscope (Olympus), was used to measure the spectra of the pure graphite powders, as described in more detail in the study by Schabel et al.^[34] Measurement spot size was 2–3 μm. Ground graphite was obtained using a mortar. All measurements were repeated at a minimum of three different positions of the powder with at least three measurements for each position.

Film Characterization: Cryo-BIB-SEM measurements of the slurries followed closely the protocol presented by Jaiser et al., with further details of the preparation procedure shown in Figure 14.^[9] All slurries were coated and immediately frozen in nitrogen slush. Still immersed in liquid nitrogen, the samples were cut perpendicular to the layers using a diamond saw. The films were then transferred to the cryo-BIB (Leica TIC3X) chamber using nitrogen-cooled vacuum transfer (Leica VCT100). The cross section was ion sputtered using three argon-ion guns at 5 kV acceleration voltage for the duration of 3–4 h removing around 50 μm material and producing a smooth and damage-free surface. The samples were transferred to the cryo-SEM while maintaining the cryo atmosphere. The capillaries of the cross section were still water filled at the given temperature of –140 °C in the cryo-SEM. By heating the chamber to –80 °C, the solvent in the surface pores sublimated, thus enabling an observation of the inner pore volume.

Expected capacities and porosities of the anodes were determined by means of area weight and thickness measurements, as well as the theoretical capacities of the graphite and the density of the electrode calculated on the basis of the recipe and the densities of the pure materials. The adhesion force of all layers was measured with a universal testing machine (AMETEK LS1) and a 90° peel test device using a 10 N load cell. All samples had a width of 30 mm and were cut perpendicular to the coating direction. Measurements of the electrical conductivity were executed with the electrodes positioned between two copper cylinders with a diameter of 40 mm. A current was applied by an E3633A power supply (Agilent Technologies) and the voltage drop was determined with a

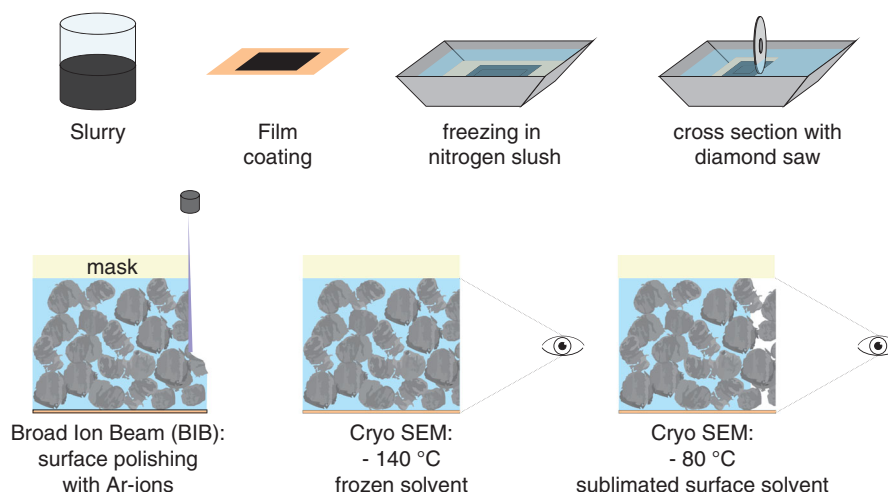


Figure 14. Preparation procedure for the cryo-BIB-SEM cross sections shown in Figure 1. The slurry is coated and directly frozen in nitrogen slush. Cross sections are prepared by a diamond saw and using BIB under cryogenic conditions. The solvent in the surface capillaries is sublimated without changing the structure of the nonvolatile components.

multimeter (2700, Keyence) using a four-wire setup and the electrical conductivity derived.

Coin Cell Preparation and Test: The anodes prepared from the four slurries as single layers or multilayers were built into full cells in coin-cell format with a minimum of three full cells for each electrode. For the cathode, NMC622 (BASF, Germany) was used as active material with an area loading of 12.15 mg cm^{-2} and a theoretical capacity of 2.0 mAh cm^{-2} . A polypropylene fleece (Adfiltec GmbH, Germany) was used as separator and the electrolyte was a mixture of EC:EMC 3:7 with 1 M LiPF_6 and 2% VC (Gelon, China). To ensure an overcapacity of the anode, the diameter of the anode was set to 16 mm and that of the cathode to 13 mm. The separator had a diameter of 17 mm. All electrodes as well as the separator were heated to 100°C for 20 min prior to cell assembly to remove remaining residual water. For the cell test, identical charging and discharging rates were applied, consisting of a formation cycle at $C/20$, two cycles at $C/10$ and two cycles at $C/5$, followed by each five cycles at $C/2$, 1C, 2C, and 3C, and followed by five cycles at $C/2$.

Supporting Information

Supporting Information is available from the Wiley Online Library or from the author.

Acknowledgements

The authors would like to thank the students involved in this work: V. Francesconi and A. Eghbalpoor. The authors acknowledge the financial support of the Federal Ministry of Education and Research (BMBF) within the “ProZell” cluster project “High Energy” under the reference number 03XP0073B and “HiStructures” within “ProZell II” under the reference number 03XP0243C. This work contributes to the research conducted at the Center for Electrochemical Energy Storage Ulm-Karlsruhe (CELEST).

Open access funding enabled and organized by Projekt DEAL.

Conflict of Interest

The authors declare no conflict of interest.

Data Availability Statement

The data that support the findings of this study are openly available in the KITopen repository “Cryo-BIB-SEM micrographs” at <https://doi.org/10.5445/IR/1000135025>

Keywords

binder migrations, drying, film formations, lithium-ion batteries, multilayers

Received: May 5, 2021

Revised: July 9, 2021

Published online:

- [1] L. Mauler, F. Duffner, J. Leker, *Appl. Energy* **2021**, *286*, 116499.
- [2] R. Diehm, M. Müller, D. Burger, J. Kumberg, S. Spiegel, W. Bauer, P. Scharfer, W. Schabel, *Energy Technol.* **2020**, *8*, 2000259.
- [3] S. Jaiser, M. Müller, M. Baunach, W. Bauer, P. Scharfer, W. Schabel, *J. Power Sources* **2016**, *318*, 210.
- [4] M. Müller, L. Pfaffmann, S. Jaiser, M. Baunach, V. Trouillet, F. Scheiba, P. Scharfer, W. Schabel, W. Bauer, *J. Power Sources* **2017**, *340*, 1.
- [5] L. Pfaffmann, S. Jaiser, M. Müller, P. Scharfer, W. Schabel, W. Bauer, F. Scheiba, H. Ehrenberg, *J. Power Sources* **2017**, *363*, 460.
- [6] B. Westphal, H. Bockholt, T. Gunther, W. Haselrieder, A. Kwade, *ECS Trans.* **2015**, *64*, 57.
- [7] B. G. Westphal, A. Kwade, *J. Energy Storage* **2018**, *18*, 509.
- [8] M. Baunach, S. Jaiser, S. Schmelzle, H. Nirschl, P. Scharfer, W. Schabel, *Drying Technol.* **2015**, *34*, 462.
- [9] S. Jaiser, J. Kumberg, J. Klaver, J. L. Urai, W. Schabel, J. Schmatz, P. Scharfer, *J. Power Sources* **2017**, *345*, 97.
- [10] H. Buqa, M. Holzapfel, F. Krumeich, C. Veit, P. Novák, *J. Power Sources* **2006**, *161*, 617.
- [11] F. Jeschull, D. Brandell, M. Wohlfahrt-Mehrens, M. Memm, *Energy Technol.* **2017**, *5*, 2108.
- [12] C.-C. Li, Y.-S. Lin, *J. Power Sources* **2012**, *220*, 413.

- [13] W. J. Chang, G. H. Lee, Y. J. Cheon, J. T. Kim, S. I. Lee, J. Kim, M. Kim, W. I. Park, Y. J. Lee, *ACS Appl. Mater. Interfaces* **2019**, *11*, 41330.
- [14] S. Lim, S. Kim, K. H. Ahn, S. J. Lee, *J. Power Sources* **2015**, *299*, 221.
- [15] H. Hagiwara, W. J. Suszynski, L. F. Francis, *J. Coat. Technol. Res.* **2014**, *11*, 11.
- [16] S. Lim, K. H. Ahn, M. Yamamura, *Langmuir: ACS J. Surf. Colloids* **2013**, *29*, 8233.
- [17] J. Drogenik, M. Gaberscek, R. Dominko, F. W. Poulsen, M. Mogensen, S. Pejovnik, J. Jamnik, *Electrochim. Acta* **2003**, *48*, 883.
- [18] R. Gordon, R. Orias, N. Willenbacher, *J. Mater. Sci.* **2020**, *257*, 421.
- [19] S. L. Morelly, N. J. Alvarez, M. H. Tang, *J. Power Sources* **2018**, *387*, 49.
- [20] R. M. Saraka, S. L. Morelly, M. H. Tang, N. J. Alvarez, *ACS Appl. Energy Mater.* **2020**, *3*, 11681.
- [21] H. Bockholt, M. Indrikova, A. Netz, F. Golks, A. Kwade, *J. Power Sources* **2016**, *325*, 140.
- [22] H. Bockholt, W. Haselrieder, A. Kwade, *ECS Trans.* **2013**, *50*, 25.
- [23] R. Diehm, J. Kumberg, C. Dörrer, M. Müller, W. Bauer, P. Scharfer, W. Schabel, *Energy Technol.* **2020**, *8*, 1901251.
- [24] D. Liu, L.-C. Chen, T.-J. Liu, W.-B. Chu, C. Tiu, *Energy Technol.* **2017**, *5*, 1235.
- [25] W. Bauer, D. Nötzel, *Ceram. Int.* **2014**, *40*, 4591.
- [26] J. Kumberg, M. Müller, R. Diehm, S. Spiegel, C. Wachsmann, W. Bauer, P. Scharfer, W. Schabel, *Energy Technol.* **2019**, *3*, 1900722.
- [27] H. Bockholt, Formulierungstechniken für eigenschaftsoptimierte Lithiumionenbatterieelektroden, Dissertationsschrift, **2016**.
- [28] M. Cerebald, B. Lestriez, R. Ferrando, A. Videoq, M. Richard-Plouet, M. T. Caldes, D. Guyomard, *Langmuir: ACS J. Surf. Colloids* **2014**, *30*, 2660.
- [29] S. H. Sung, S. Kim, J. H. Park, J. D. Park, K. H. Ahn, *Materials* **2020**, *13*, 4544.
- [30] P. Smyrek, J. Pröll, H. J. Seifert, W. Pfleging, *J. Electrochem. Soc.* **2015**, *163*, A19.
- [31] W. Pfleging, *Nanophotonics* **2018**, *7*, 549.
- [32] M. Baunach, S. Jaiser, P. Cavadini, P. Scharfer, W. Schabel, *J. Coat. Technol. Res.* **2015**, *12*, 915.
- [33] J. Kumberg, M. Baunach, J. C. Eser, A. Altvater, P. Scharfer, W. Schabel, *Energy Technol.* **2020**, *3*, 2000889.
- [34] W. Schabel, *Chem. Ing. Tech.* **2005**, *77*, 1915.